

## 3.9 THz spatial filter based on a back-to-back Si-lens system

YUNER GAN,<sup>1,2,6</sup>  BEHNAM MIRZAEI,<sup>1,3</sup> SEBASTIAAN VAN DER POEL,<sup>4</sup> JOSE R. G. SILVA,<sup>1,2</sup> MATVEY FINKEL,<sup>1</sup> MARTIN EGGENS,<sup>1</sup> MARCEL RIDDER,<sup>1</sup> ALI KHALATPOUR,<sup>5</sup> QING HU,<sup>5</sup> FLORIS VAN DER TAK,<sup>1,2</sup> AND JIAN-RONG GAO<sup>1,3,7</sup>

<sup>1</sup>*SRON Netherlands Institute for Space Research, Groningen/Utrecht, 9747 AD/3584 CA, The Netherlands*

<sup>2</sup>*Kapteyn Astronomical Institute, University of Groningen, Groningen, 9747 AD, The Netherlands*

<sup>3</sup>*Optics Research Group, Department of Imaging Physics, Delft University of Technology, Delft, 2628 CJ, The Netherlands*

<sup>4</sup>*Kavli Institute of Nanoscience, Department of Quantum Nanoscience, Delft University of Technology, Delft, 2628 CJ, The Netherlands*

<sup>5</sup>*Department of Electrical Engineering and Computer Science, Massachusetts Institute of Technology, Cambridge, MA 02139, USA*

<sup>6</sup>*y.n.gan@sron.nl*

<sup>7</sup>*j.r.gao@sron.nl*

**Abstract:** We present a terahertz spatial filter consisting of two back-to-back (B2B) mounted elliptical silicon lenses and an opening aperture defined on a thin gold layer between the lenses. The beam filtering efficiency of the B2B lens system is investigated by simulation and experiment. Using a unidirectional antenna coupled 3rd-order distributed feedback (DFB) quantum cascade laser (QCL) at 3.86 THz as the source, the B2B lens system shows 72% transmissivity experimentally with a fundamental Gaussian mode as the input, in reasonably good agreement with the simulated value of 80%. With a proper aperture size, the B2B lens system is capable of filtering the non-Gaussian beam from the QCL to a nearly fundamental Gaussian beam, where Gaussicity increases from 74% to 99%, and achieves a transmissivity larger than 30%. Thus, this approach is proven to be an effective beam shaping technique for QCLs, making them to be suitable local oscillators in the terahertz range with a Gaussian beam. Besides, the B2B lens system is applicable to a wide frequency range if the wavelength dependent part is properly scaled.

© 2020 Optical Society of America under the terms of the [OSA Open Access Publishing Agreement](#)

### 1. Introduction

Heterodyne detection, which makes use of a mixing detector and a high power local oscillator (LO), measures the light intensity together with an exceptionally high spectral resolution. In astronomy, this technique is widely used to study atomic fine structure lines and molecular rotational lines at terahertz frequencies (0.1-10 THz) [1]. At supra-terahertz frequencies (> 1 THz), the available heterodyne detectors include Schottky diodes [2], hot electron bolometers (HEB) [3], terahertz quantum well photodetectors (QWP) [4], and quantum cascade laser (QCL) detectors, which can be used for dual-comb multiheterodyne detection [5–7]. HEB mixers, due to their high sensitivity, are the choice of heterodyne detector for astrophysics. Waveguide-based HEB mixers have been used up to 4.7 THz in the heterodyne spectrometers GREAT (German Receiver for Astronomy at Terahertz frequencies) and upGREAT on the Stratospheric Observatory for Infrared Astronomy (SOFIA) [8]. In the frequency range > 1 THz, a quasi-optical approach based on a lens-antenna is commonly used to couple THz radiation from an LO source to a detector [3]. Typically a THz quantum cascade laser (QCL) acts as the LO, while the mixer is a superconducting HEB, integrated with a planar antenna on a lens [9]. Additionally, to match

the beam from the source to the mixer, a few lenses or reflective mirrors are included in the optical path. A QCL is the most promising LO source at supra-terahertz frequencies due to its high output power. Current THz QCLs have been demonstrated to cover the frequency range from 1.2 THz to 5.0 THz, and their output powers reach more than 200 mW in continuous-wave mode and watt level in pulsed mode [10–13], which is sufficient as an LO for a heterodyne array with more than 100 mixers. One of the QCL designs, the third order distributed-feedback (DFB) laser structure based on double metal waveguide designs, is being implemented for heterodyne instruments, with a single-mode emission, a high-temperature operation, and a relatively narrow beam [14]. The angular divergence of its beam is  $\sim 10^\circ$  and  $\sim 25^\circ$  in orthogonal directions, which are within  $30^\circ$  from the propagation axis, meeting the criterion of the validity of the paraxial approximation when using a Gaussian optics analysis according to [15]. However, the beams of QCLs deviate considerably from a fundamental Gaussian shape. A fundamental Gaussian beam is essential in terms of effective coupling of the radiation to lens-antenna mixers, the far field of which is nearly fundamental Gaussian beam [16,17]. Furthermore, it reduces stray light, caused by reflections from optical components, and makes the optical design for an instrument system more accurate. In order to improve mapping speed, heterodyne array receivers with multiple mixers at supra-THz frequencies have been developed, e.g. for the Galactic/Extragalactic ULDB Spectroscopic Terahertz Observatory (GUSTO) and the Stratospheric Observatory for Infrared Astronomy (SOFIA) [18,19]. For heterodyne mixer arrays, phase gratings are used as the multiplexer, which diffracts a single QCL beam into multiple beams as an array LO [20] and recently reported up to 81 beams [21]. To avoid overlap between the individual diffracted beams, a Gaussian input beam to the grating is required [22,23].

QCL based on the surface plasmon design has a better output beam, but has the disadvantage of a relatively low operation temperature. Such an approach has been successfully implemented for the 4.7 THz heterodyne spectrometer GREAT on SOFIA although the beam still contains higher-order Gaussian modes [24]. Hollow waveguides or hyper-hemispherical silicon lenses mounted near the exit facet of the QCLs inside the cryostat window achieve a far field single-lobe beam pattern with low divergence, but the beam profile is not ideal and the mechanical robustness can be a concern [25–28]. A combination of a spherical lens and a diaphragm has been used to produce a directive beam with the uniform phase front, from a wire laser [29]. The latter is known to produce a divergent, undirective beam. We are interested in introducing a spatial filter for a THz QCL to form a THz source with not only a high power, but also a fundamental Gaussian beam. A known beam filter is a back-to-back corrugated feedhorn pair, which has been used as a spatial filter to eliminate the high-order Gaussian modes and random fluctuations of a source at microwave frequencies [30]. Such a feedhorn pair has been also manufactured at 2.5 THz and shows an excellent beam pattern [31]. However, the feed horn approach requires precise fine structures to obtain a fundamental Gaussian beam, which is difficult to manufacture at high THz frequencies. Besides, such a structure is inherently narrowband. Therefore, developing a beam filter capable of shaping a non-Gaussian beam into a fundamental Gaussian beam with a good efficiency is highly demanded.

In this work, we report a spatial filter based on a back-to-back (B2B) lens system operated at a supra-THz frequency and its characterization using an available high power QCL at 3.9 THz. The beam filtering efficiency of the B2B lens system, which characterizes both the Gaussianity of the output beam and power transmissivity, is studied in both simulation and experiment. Besides, a mechanical lens holder is introduced to align the lens system for optimal performance. Because the available source in our study has a frequency of 3.9 THz, our simulation and experiment will focus on this particular frequency. However, the B2B lens system should be applicable for different wavelengths if the wavelength dependent part is properly scaled.

## 2. Device concept and analysis

### 2.1. Back-to-back lens system

A conventional spatial filter is composed of three separate components, a lens, a pinhole, and a lens [32]. In analogy to that, our B2B lens system is an integrated lens system, where two back-to-back elliptical lenses [33] are contacted via an aperture etched in a thin Au layer, to reduce the silicon-air interfaces through which THz light travels. Thus, the efficiency of the spatial filter is enhanced. One can use a lens and an iris aperture to achieve a quasi-Gaussian beam, as our group did in [21], but the efficiency is very low ( $\sim 10\%$ ). Two off-axis parabolic mirrors combined with a pinhole can also be used as a beam filter with an efficiency of 22% [22], but the system is bulky and the alignment of the whole system is challenging. In our approach, a lens with an elliptical front surface is chosen because it couples well to a Gaussian-beam at its minimum waist [34] and its on-axis beam has no aberrations if the eccentricity is equal to the reciprocal of the refractive index of the lens material [35]. The spatial filter configuration and filtering principle are schematically illustrated in Fig. 1, where an imperfect laser beam is firstly focused on the focal point of the first lens, the aperture with an appropriate diameter blocks the undesired part of the laser beam, and then the second lens re-collimates the laser beam. In detail, a B2B lens system consists of two high-resistivity ( $> 5 \text{ k}\Omega\text{cm}$ ) silicon (HRSi) lenses, between which is a piece of a double-side polished HRSi wafer coated with a thin gold layer on one side. Here a circular hole, used as the aperture, is lithographically defined in its center that lets only a certain part of the beam pass through. Since gold is highly reflective, it blocks the undesired light from the incoming beam. A thin Ti layer is used for the adhesion of gold on the silicon wafer-piece. The thickness of the gold layer is  $200 \pm 3 \text{ nm}$ , which is much larger than the penetration depth of  $\sim 40 \text{ nm}$  of gold at 3.9 THz. A Si elliptical lens with a 10 mm diameter has been demonstrated to have a good performance when used in a lens antenna [36]. In the B2B lens system, the two lenses have the same diameter of 10 mm and a semi-major axis of 5.23 mm. The lens on the left in Fig. 1 has an extension of 1.53 mm to focus the incoming beam to its second focal point, while the lens on the right has a reduced extension of 1.25 mm combining with the wafer-piece of 0.28 mm thick, making the focal point at the same position as for the left lens. The wafer-piece is a  $10.5 \times 10.5 \text{ mm}^2$  square to cover the entire back surface of the lenses. The optical transmissivity of the air-silicon interface is  $\sim 70\%$  [37], causing the total transmissivity of the double lens system to be  $\sim 50\%$ . To reduce reflection losses, an anti-reflection layer is deposited on the surface of the Si lens. Ideally, the reflection of the incoming beam into a Si lens is reduced to zero at normal incidence if the refractive index and the thickness satisfy the following relations [37]:

$$n_{AR} = \sqrt{n_{Si}}, \quad (1)$$

$$t_{AR} = \frac{(2m+1)\lambda}{4n_{AR}} (m = 0, 1, 2, \dots), \quad (2)$$

where  $n_{AR}$  is the refractive index of the anti-reflection coating,  $n_{Si}$  is the refractive index of silicon,  $\lambda$  is the wavelength of the incoming beam, and  $t_{AR}$  is the thickness of the anti-reflection coating. A common choice is Parylene C, which is a thermoplastic polymer with good thermal stability and adhesion properties. Parylene C has a refractive index of about 1.62, which is close to the ideal value of 1.85, and has the advantage of being able to coat on small and curved optics with almost any thickness and with high homogeneity [38]. The thicknesses of the Parylene C coatings on the two lens surfaces are measured to be  $11 \pm 1 \mu\text{m}$ , which is about a quarter of the wavelength of 3.9 THz radiation in Parylene C. When the two lenses and the wafer-piece all are aligned well and contact tightly, without air gaps between the lenses and the wafer-piece, the transmissivity of the lens system is calculated to be 92% using the Fresnel equation [39]. The 8% losses are due to the oblique incidence to the elliptical surface and the difference between the refractive index 1.62 of Parylene C and the ideal refractive index 1.85. However, the absorption coefficients of Parylene C

[40] and HRSi need to be considered. Taking the absorption coefficients of Parylene C of  $25 \text{ cm}^{-1}$  [37] and the absorption coefficient of HRSi of  $0.05 \text{ cm}^{-1}$  [41] into account, the transmissivity of the lens system is simulated with COMSOL Multiphysics as explained in the next section.

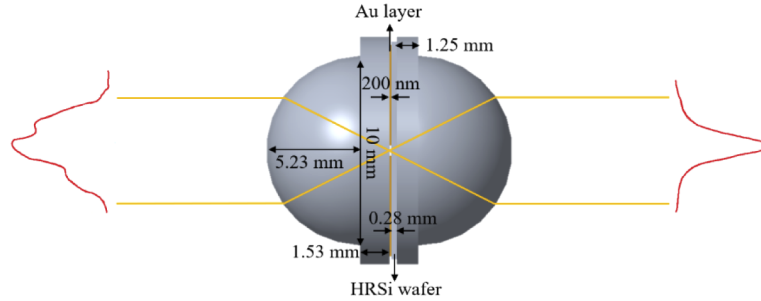


**Fig. 1.** Back-to-back lens system containing two Si lenses and a Si wafer-piece deposited with a thin gold layer. The three components are aligned together. The incoming non-Gaussian beam is first focused by the left lens, then the gold layer blocks the unwanted part. After the right lens a Gaussian beam is obtained.

## 2.2. Simulation and expected results

In COMSOL Multiphysics [42], a 2D model of the B2B lens system, shown in Figs. 2(a) and 2(b), is created to simulate its filtering efficiency. Due to the overloaded calculation for the 10 mm diameter lenses at 3.86 THz, the lenses are rescaled to 4 mm in diameter to facilitate the simulation. In this case, the size of the wafer-piece and the incoming beam are also rescaled proportionally [43]. The incident Gaussian beam is assigned by an input port with a perfectly matched layer (PML), which absorbs the reflected waves. The aperture is simulated by assigning the two boundaries beside the hole as perfect electric conductors (PECs), which reflect waves back totally. With an aperture presented, as in Fig. 2(b), part of the wave is reflected back compared to the system without an aperture in Fig. 2(a). Therefore, the presence of the aperture influences the transmissivity of the lens system and its output beam profile. The extent of influence depends on the size of the aperture, which will be described later.

With a bare wafer-piece (no PECs assigned) placed in the middle of the lenses and a fundamental Gaussian beam as the input, the output beam is a fundamental Gaussian beam. The transmissivity of the lens system, which is defined as the ratio between the output power from the lens system and the input power, is simulated to be 80% with the anti-reflection coating of Parylene C. Compared to the value of 92% in Section 2.1, the loss of 12% is due to the absorption of Parylene C and HRSi. The transmissivity of the lens system without the AR coating is only 49%, implying that the AR coating improves the transmissivity by 31%.

A proper aperture size is essential to effectively filter a non-Gaussian beam into a fundamental Gaussian beam. Let the electric field distribution of the incoming beam be  $U(P_0)$ , which is in the  $xy$  plane as shown in Fig. 2(c) and its distribution is within a surface  $S_0$ . Using the first Rayleigh–Sommerfeld diffraction formula [44] the field distribution  $U(P_1)$  on the surface of the first elliptical lens can be expressed as:

$$U(P_1) = \frac{i}{\lambda} \iint_{S_0} U(P_0) \cos(\vec{n}_1, \vec{r}_1) \frac{\exp(ikr_1)}{r_1} dS_0. \quad (3)$$

Here,  $\vec{n}_1$  is the normal vector of the surface  $S_0$ ,  $\vec{r}_1$  is the vector from  $P_0$  to  $P_1$ ,  $k$  is the wave number  $2\pi/\lambda$ , and  $r_1$  is the length of the vector  $\vec{r}_1$ . Since the first Rayleigh–Sommerfeld diffraction formula requires the diffracting screen to be planar, the more general Fresnel-Kirchhoff

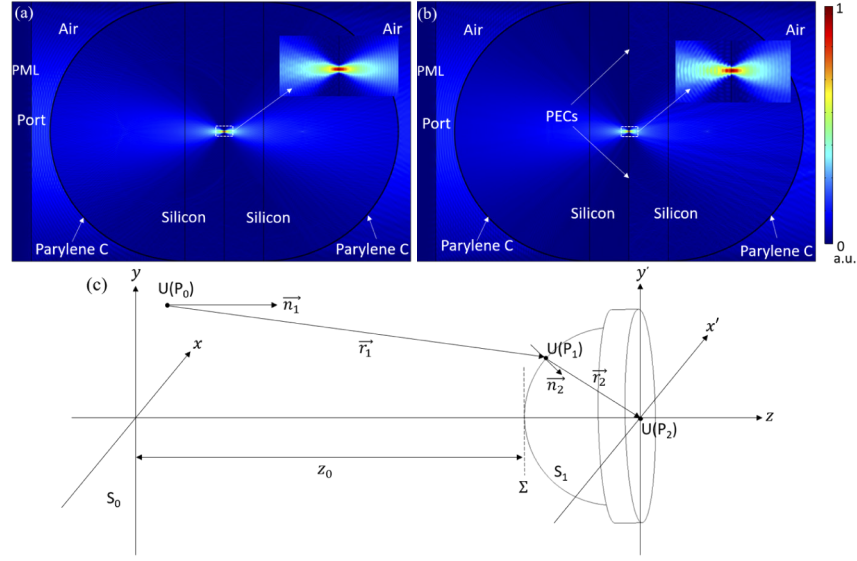


**Fig. 2.** (a) 2D model of the B2B lens system without apertures in simulation. Different colors indicate the electric field distribution. The inset is the field distribution around the focal point of the lens system. (b) 2D model of the B2B lens system with an aperture in simulation. (c) Schematic of field propagation from the  $xy$  plane to the  $x'y'$  plane.

diffraction formula [44] is used to calculate the field distribution  $U(P_2)$  on the focal plane  $x'y'$  of the elliptical lens,

$$U(P_2) = \frac{i}{2\lambda} \iint_{S_1} U(P_1) [\cos(\vec{n}_2, \vec{r}_1) + \cos(\vec{n}_2, \vec{r}_2)] \frac{\exp(ikr_2)}{r_2} dS_1, \quad (4)$$

$$I(P_2) = |U(P_2)|^2, \quad (5)$$

where  $S_1$  is the surface of the elliptical lens,  $\vec{n}_2$  is the normal vector of the surface  $S_1$ , is the vector pointing from  $P_1$  to  $P_2$ , and  $r_2$  is the length of the vector  $\vec{r}_2$ . Computing these two integrals, from the incoming field distribution the field distribution and the beam size on the focal plane of the elliptical lens are obtained. The proper aperture size should be close to the beam size on the focal plane. However, it is difficult to know the field distribution of QCL beams in advance, which deviate from a Gaussian distribution to varying degrees. So our approach is first to fit the nearly collimated non-Gaussian QCL beam in the plane  $\Sigma$  in Fig. 2(c) with the Gaussian equation [15] and derive an estimated beam waist  $\omega_{0x}$  and  $\omega_{0y}$  (defined as the radius at which the amplitude is  $1/e$  of its peak value) in the orthogonal direction. Then the electric field distribution  $U(P_0)$  of this fitted Gaussian beam in the  $xy$  plane [45] in Fig. 2(c) is substituted in Eqs. (3)–(5) to calculate the corresponding field distribution in the focal plane, from which the proper aperture size is estimated:

$$U(P_0) = \sqrt{\frac{2}{\pi\omega_x\omega_y}} \exp\left(-\frac{x^2}{\omega_x^2} - \frac{y^2}{\omega_y^2}\right), \quad (6)$$

$$\omega_x = \omega_{0x} \sqrt{1 + \left(\frac{\lambda z_0}{\pi\omega_{0x}^2}\right)^2}, \quad (7)$$

$$\omega_y = \omega_{0y} \sqrt{1 + \left(\frac{\lambda z_0}{\pi\omega_{0y}^2}\right)^2}. \quad (8)$$

To verify the filtering efficiency of the B2B lens system with apertures, a Gaussian beam with sidelobes indicated with the black dashed line (a far field plot) in Fig. 3 is used as the input beam. Fitting this beam with the Gaussian equation, the waist of the fitted Gaussian beam at the plane  $\Sigma$  is found to be  $\sim 1.7$  mm. We then calculate the waist of the Gaussian beam in the focal plane by using Eqs. (3)–(8) with  $\omega_{0x}=\omega_{0y}=1.7$  mm. We find the beam waist to be  $13.8$   $\mu\text{m}$ , indicating that the proper aperture diameter is around  $28$   $\mu\text{m}$ . Figure 3 plots the intensity profiles of the output beams in the far field from the B2B lens system with different aperture diameters, which are simulated by COMSOL. In the case of the bare wafer-piece (no aperture), the output beam profile is similar to the input with a reduced power level. By reducing the aperture size from  $40$  to  $10$   $\mu\text{m}$ , the level of the sidelobes in the output beam is affected and starts to be suppressed when the size is  $30$   $\mu\text{m}$ , confirming the role of the aperture. It is important to notice that the transmissivity decreases as well. We concentrate on filtering a QCL output to a beam that can better couple to a lens-antenna coupled HEB mixer, which is known to have a Gaussian beam, and one of the impact factors for the coupling efficiency is the Gaussicity of the beam. Therefore, the transmissivity of the B2B lens system and the Gaussicity of the output beam are two main characterizations for the lens system. The transmissivities of the B2B lens system with different aperture sizes and the corresponding Gaussivities [46,47] of the output beams are calculated and summarized in Table 1. Combining the intensity profiles in Fig. 3 with the transmissivities and Gaussivities in Table 1, we find that the B2B lens system shows good performance when the aperture diameter is between  $15$   $\mu\text{m}$  and  $30$   $\mu\text{m}$ , which agrees well with the estimated aperture diameter of  $28$   $\mu\text{m}$ .

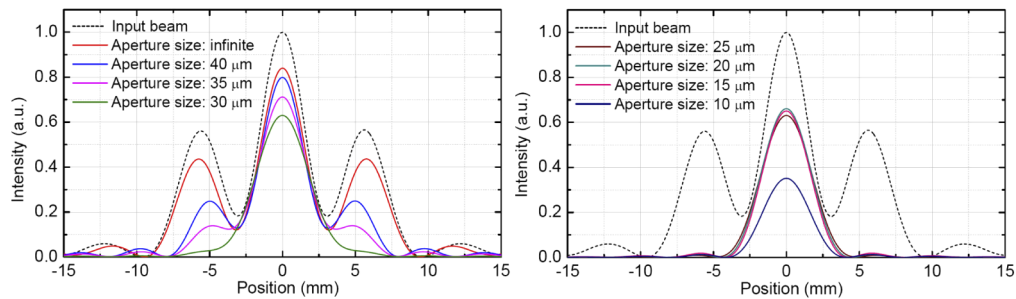


**Fig. 3.** Intensity profiles of the output beams from the back-to-back lens system with different aperture sizes at the far field. The black solid line indicates the output beam profile from the lens system when there is no gold layer between two lenses. Its profile is identical to the input beam profile, which is indicated with the black dashed line. For better comparison, all intensity values have been divided by the maximum intensity of the input beam.

**Table 1. Transmissivities and Gaussivities of the B2B lens system with different aperture sizes at 3.86 THz.**

Aperture size	No aperture	40 $\mu\text{m}$	35 $\mu\text{m}$	30 $\mu\text{m}$	25 $\mu\text{m}$	20 $\mu\text{m}$	15 $\mu\text{m}$	10 $\mu\text{m}$
Transmissivity	80.4%	57.3%	48.3%	36.4%	32.5%	32.9%	31.9%	17.2%
Gaussicity	38.7%	79.9%	93.5%	99.8%	99.9%	99.8%	99.7%	99.6%

Choosing an appropriate aperture size is also important to effectively filter the higher order Gaussian modes. For instance, if there is a  $\text{TEM}_{11}$  mode with  $\omega_{0x}=\omega_{0y}=1.5$  mm beam waist present in the incoming beam, according to Eqs. (7)–(8) its field distribution is expressed as:

$$U(P_0) = \sqrt{\frac{2}{\pi\omega_x\omega_y}} \frac{xy}{\omega_x\omega_y} \exp\left(-\frac{x^2}{\omega_x^2} - \frac{y^2}{\omega_y^2}\right). \quad (9)$$

Taking this field into Eqs. (3)–(5), the intensity distribution of the beam on the focal plane is obtained. We find that the proper aperture diameter to block this beam is smaller than 14  $\mu\text{m}$ . Table 2 illustrates the simulated transmissivities of the B2B lens system to a  $\text{TEM}_{11}$  Gaussian mode when the aperture size changes from 20  $\mu\text{m}$  to 12  $\mu\text{m}$ . This Gaussian mode is nearly fully blocked by the aperture when its size is smaller than 14  $\mu\text{m}$ . The B2B lens system is therefore capable of filtering higher order Gaussian modes when the aperture diameter is properly chosen.

**Table 2. Transmissivities of the B2B lens system with different aperture sizes for  $\text{TEM}_{11}$  Gaussian mode.**

Aperture size	20 $\mu\text{m}$	18 $\mu\text{m}$	16 $\mu\text{m}$	14 $\mu\text{m}$	12 $\mu\text{m}$
Transmissivity	18.3%	7.7%	2.8%	0.76%	0.19%

### 3. Mechanical lens holder and measurement setup

#### 3.1. Mechanical lens holder and alignment procedure

As suggested by the simulations in Section 2, with the lens system well aligned, the transmissivity of the lens system reaches 80.5% for a bare wafer-piece with a fundamental Gaussian input beam. However, once there are air gaps between the wafer-piece and the lenses, the performance degrades and the transmissivity decreases quickly. In practice, the transmissivity remains higher than 70% if the air gap is below 2  $\mu\text{m}$ . Another important issue is that the centers of the two lenses (or the optical axis) and the center of the aperture should be well aligned, otherwise the performance degrades too. The required accuracy depends on the aperture size. According to the simulation, for the 10- $\mu\text{m}$  diameter aperture, the transmissivity changes only 2% if there is 1  $\mu\text{m}$  misalignment. For an enlarged aperture, which will be discussed later on, the effect is smaller and becomes negligible. Therefore, our goal is to keep the misalignment as low as 1  $\mu\text{m}$ . A mechanical lens holder is designed dedicatedly to align the lens system to such accuracy. By combining the mechanical lens holder with micromanipulators and a microscope, we can realize an alignment accuracy of 1  $\mu\text{m}$ . The mechanical lens holder and micromanipulators are described in Appendix A, together with a description of the alignment procedure.

#### 3.2. THz QCL and measurement setup

To measure the filtering efficiency of the B2B lens system, a unidirectional antenna-coupled third order distributed feedback (DFB) quantum cascade laser (QCL) at 3.86 THz is applied as a source [14]. Figure 4(a) shows an SEM photo of the laser structure, and the simulated far-field radiation pattern together with the electric field distribution inside the laser in Fig. 4(b). The addition of a “reflector” structure is to redirect the power in the undesired backward direction to the desired forward direction, and thus increasing the output power of this laser by a factor of  $\sim 2$  over a usual bidirectional QCL. The laser used has about 10 mW output power, which is relatively high and favorable for obtaining a high signal to noise ratio in the 2D beam profile measurements. Furthermore, the third order DFB structure improves the output beam pattern, namely less divergent, as shown in Fig. 4(c). The beam size is  $\sim 25$  mm in the vertical direction (parallel to the QCL plane) and  $\sim 15$  mm in the horizontal direction, implying an angular full width at half-maximum (FWHM) of  $23^\circ$  and  $14^\circ$  in the respective directions. Obviously, the beam deviates considerably from a fundamental Gaussian beam profile.

Figures 5(a) and 5(b) illustrate the measurement setup schematically, where two versions with different optics between the QCL and the B2B lens system. The setup in Fig. 5(a) is used to measure the transmissivity of the B2B lens system with a bare Si wafer-piece. The QCL is cooled down to  $\sim 10$  K in a pulsed tube cooler. The emitted beam is collimated by a high-density polyethylene (HDPE) lens and filtered by an iris aperture to produce a Gaussian-like input beam

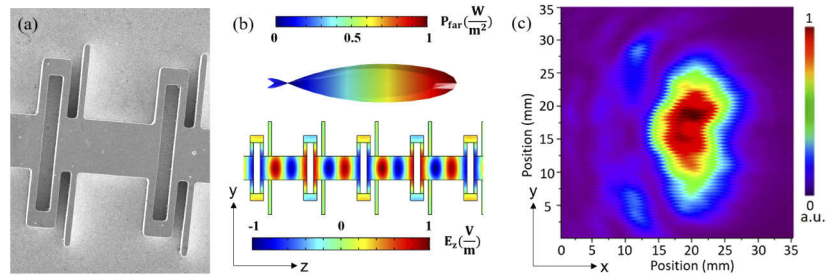


**Fig. 4.** (a) SEM micrograph of the 3rd-order DFB QCL. (b) Simulated far-field radiation pattern (top) and the corresponding electric field distribution inside the laser (bottom) in arbitrary units. (c) Measured output beam pattern from the QCL in the plane perpendicular to the laser structure in (b) at a distance 3.5 cm from the exit of the QCL. Here  $y$  is the vertical direction, being parallel to the QCL plane, while  $x$  is the horizontal direction, being perpendicular to the QCL chip.

profile with a 3.5 mm beam waist. The iris aperture can produce a nearly Gaussian distributed beam, but the efficiency in this case is so low that most of the power ( $\sim 90\%$ ) from the QCL is blocked. A pyro-electric detector mounted on a 2D scanner stage is used to map the beam pattern. The B2B lens system is mounted on a kinematic mount with adjustable angles in the orthogonal directions, and this mount is installed on a 3-axis precision stage, being able to adjust the position of the lens system with 0.1 mm accuracy. As the first step, the peak intensity of the incoming Gaussian-like beam is measured with the detector. Then, the detector position is fixed.

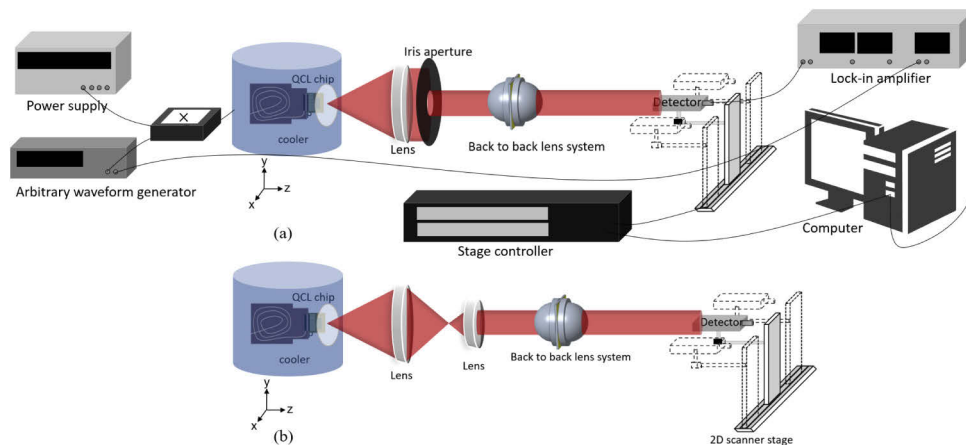


**Fig. 5.** (a) Measurement setup for testing the transmissivity of the lens system without the gold blocking layer. The QCL is mounted vertically in a pulse tube cooler (cooled to  $\sim 10$  K) and its bias voltage is modulated by a sinusoidal function at 70 Hz using an arbitrary waveform generator. The QCL beam is first collimated by an HDPE lens and filtered by an iris aperture, then goes through the lens system. A pyro-electric detector mounted on a 2D scanner stage is used to map the beam pattern. The received signal is read out by a lock-in amplifier with a 70 Hz sinusoidal function reference. The computer controls the stage and reads out the signal received from the lock-in amplifier. (b) Measurement setup for testing the filtering efficiency of the lens system with different aperture sizes. The QCL beam size is reduced by two high-density polyethylene lenses before the beam goes through the lens system.

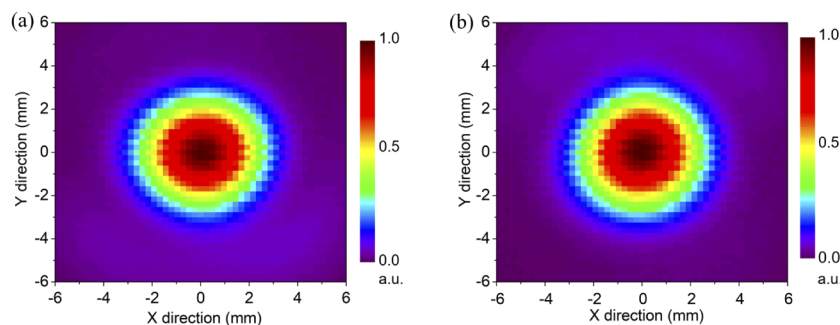
Subsequently, the first surface of the lens system is placed on the beam waist position of the incoming beam, which is 5 cm away from the iris aperture. The positions and angles of the lens system are fine-tuned by the mounted stage until the peak intensity of the output beam is at the same position as the peak intensity of the input beam. In this way, the lens system is well aligned with the input beam. The output beam pattern is scanned at a plane that is 8.6 cm away from the 2nd surface of the lens system (15 cm away from the iris aperture since the length of the lens system is 1.4 cm). After removing the lens system, the detector is moved 1.4 cm closer to the iris aperture to make sure that the optical path in the air is the same, and thus the losses in two cases are the same when calculating the transmissivity of the lens system. Then in this position, the input beam pattern is measured.

Figure 5(b) shows the second version of the setup to test the filtering efficiency of the lens system. Two HDPE lenses are introduced to make the input beam size smaller than the lens diameter. Using the same alignment method as described before, several output beam patterns from the lens system with different aperture sizes and the input beam pattern at the position mentioned above are scanned to calculate the transmissivity of the lens system. The input beam pattern at the plane of the first surface of the lens system (the beam waist position) is also scanned to compare the beam shape change from the input to the output beam.

## 4. Measurements and analysis

### 4.1. Transmissivity of the B2B lens system without an opening aperture

The transmissivity of the lens system with a bare wafer-piece is studied to verify the lens system as well as the AR coating. Figure 6(a) shows intensity image plots of the input Gaussian-like beam and the output beam from the lens system is shown in Fig. 6(b), where the color corresponds to the intensity. The output beam has almost the same size as the input beam, but vertically and horizontally flipped due to the light propagation inside the lens system. After removing the noise floor caused by the pyro-electric detector itself in both the output beam and the input beam data, the transmissivity is calculated to be 72%, which is lower than 80% from the simulation. The difference is only 8%, therefore the measured transmissivity is an excellent result if the possible loss due to the air gaps, tilt angle, and the offset is taken into account.



**Fig. 6.** (a) Intensity image plot of the input beam. (b) Intensity image plot of the output beam from the lens system without the gold layer. The color indicates relative intensity.

As explained in the following analysis, any of the mentioned factor affects the transmissivity. Firstly, although we try to minimize the air gaps between the lenses and the wafer-piece, they cannot be fully removed. To obtain a quantitative impression, the transmissivity change as a function of the air gap size is calculated based on the Fresnel equation [39] and plotted in Fig. 7(a). To account for the 8% reduction, the two air gaps will roughly be 2  $\mu\text{m}$ . Secondly, there might be a tilt angle between the beam propagation direction and the optical axis of the lens system. The

change of the transmissivity as a function of the tilt angle is simulated and shown in Fig. 7(b), where the transmissivity change is slow and is reduced by 8% if the tilt angle reaches  $12^\circ$ . Finally, there might be an offset between the center of the beam (peak intensity) and the center of the lens system. Figure 7(c) shows the simulated transmissivity change as a function of the offset, where to account for the 8% reduction, the offset reaches about 36% of the lens diameter, being 3.6 mm. It is likely that the air gaps are the dominant cause for the 8% reduction in transmission. This is based on the simulations and experimental experience, from which we know that much smaller values of the tilt angle and the offset can be achieved. During the measurement, the humidity change in the lab could also influence the results, which is estimated to be  $<1\%$ , so it can be neglected.

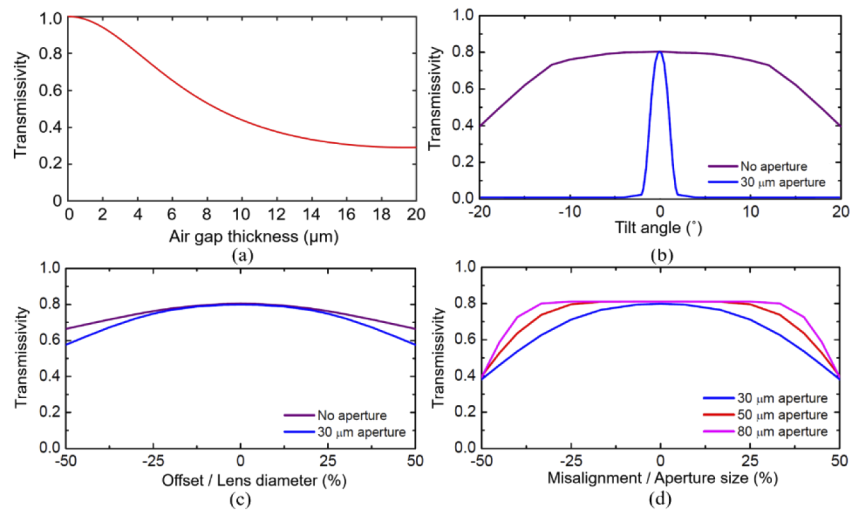


**Fig. 7.** (a) Transmissivity of the back-to-back lens system changes with the thickness of the two air gaps between the lenses and the wafer-piece. (b) Simulated transmissivity changes with a tilt angle between the direction of the beam and the optical axis of the lens system. (c) Simulated transmissivity as a function of the ratio of the offset between the center of the beam and the center of the lens system to the lens diameter. The purple line in (b) and (c) indicates the transmissivity change when there is no aperture between two lenses, and the blue line indicates the transmissivity change when the aperture size is  $30\ \mu\text{m}$ . (d) Simulated transmissivity change as the function of the ratio of the misalignment between the aperture center and the lens center and to aperture size. The red, blue, and magenta lines indicate the transmissivity changes when the aperture diameter is  $30\ \mu\text{m}$ ,  $50\ \mu\text{m}$ ,  $80\ \mu\text{m}$ , respectively.

#### 4.2. Filtering efficiency of the B2B lens system with an opening aperture

The bare wafer-piece is replaced by the pieces with different sizes of the aperture to test the filtering efficiency of the B2B lens system. In the meantime, the input beam is changed to a non-Gaussian beam, which originates from the same QCL. Since the QCL beam is divergent, its beam size becomes larger than the diameter of the lens system even at the position of the cryostat window. Therefore, two HDPE lenses are necessary to collimate the beam and adjust its size. The beam pattern, measured after the two lenses, is plotted in Fig. 8(a), where Fig. 8(a<sub>1</sub>) shows the beam intensity pattern on the linear scale and (a<sub>2</sub>) shows the two 1D cuts in the diagonal and anti-diagonal directions on the decibel scale. They confirm the non-Gaussian distribution, but the beam becomes more symmetric compared to the original beam taken directly from the QCL as shown in Fig. 4(c). The reason is that due to the limited diameter of the first lens in Fig. 5(b) the outer part of the QCL beam is not collected. As described in Section 2, we fit

this beam with a Gaussian profile, derive beam waists in two directions ( $\omega_{0x}=3.3$  mm,  $\omega_{0y}=3.8$  mm), and get the beam waist ( $\omega_x=16.3$   $\mu\text{m}$ ,  $\omega_y=15$   $\mu\text{m}$ ) in the focal plane by Eqs. (3)–(5). Thus, the optimal aperture size for filtering this beam is expected to be around 30  $\mu\text{m}$ . An aperture much larger than this size is not capable of filtering the undesired components, and an aperture much smaller than this size blocks the desired components of the beam. Figures 8(b<sub>1</sub>), 8(c<sub>1</sub>), and 8(d<sub>1</sub>) plot the output beam intensity patterns with 30  $\mu\text{m}$ , 50  $\mu\text{m}$ , and 80  $\mu\text{m}$  aperture size on a linear scale, respectively, and Figs. 8(b<sub>2</sub>), 8(c<sub>2</sub>), and 8(d<sub>2</sub>) plot their 1D cuts in the diagonal and anti-diagonal directions on a decibel scale. When the size-shaped beam propagates through the lens system with the 30  $\mu\text{m}$  aperture, as shown in Fig. 8(b), the output beam is much improved and becomes circular. With the aperture size increases to 50  $\mu\text{m}$  and 80  $\mu\text{m}$ , the output beams become less circular and begin to deviate from a fundamental Gaussian beam. Due to the long scanning time, only the main part of the output beam is measured, but the sidelobe level in the output beam is found to be low  $\sim -20$  dB from Fig. 8(b<sub>2</sub>). To quantify the filtering efficiency by different apertures, the transmissivities and Gaussivities of the B2B lens system are calculated and summarized in Table 3.

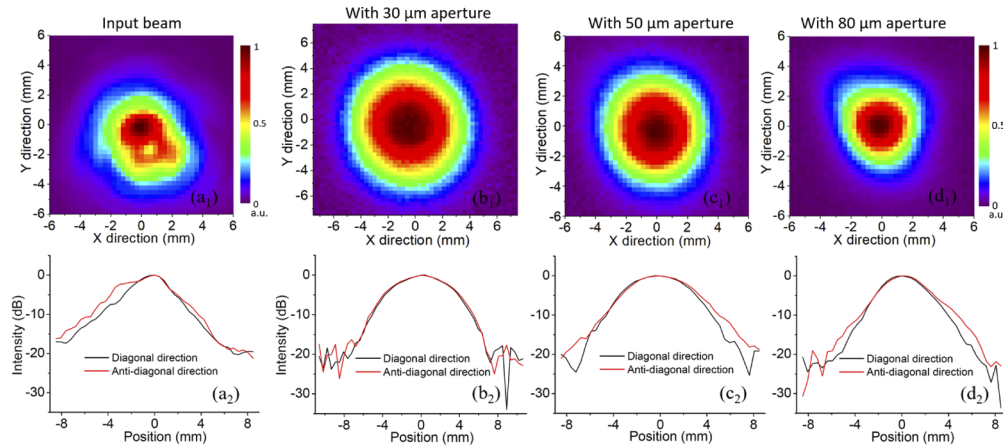


**Fig. 8.** (a<sub>1</sub>)(a<sub>2</sub>) Intensity plot of the input beam in the plane of the first surface of the lens system on the linear scale and its 1D profiles in the diagonal and anti-diagonal directions on the decibel scale. (b<sub>1</sub>)(c<sub>1</sub>)(d<sub>1</sub>) Intensity plots of the output beams from the lens system at a distance 8.6 cm away from the last surface of the lens system on the linear scale when the aperture diameter is 30  $\mu\text{m}$ , 50  $\mu\text{m}$ , and 80  $\mu\text{m}$ , respectively. They share the same color scale. (b<sub>2</sub>)(c<sub>2</sub>)(d<sub>2</sub>) 1D profiles of the output beams in the diagonal and anti-diagonal directions on the decibel scale when the aperture size is 30  $\mu\text{m}$ , 50  $\mu\text{m}$ , and 80  $\mu\text{m}$ , respectively. They share the same y label.

**Table 3. Transmissivities and Gaussivities of the lens system with different aperture sizes at 3.86 THz.**

Aperture size	30 $\mu\text{m}$	50 $\mu\text{m}$	80 $\mu\text{m}$	No aperture
Transmissivity	31%	34%	43%	72%
Gaussivity	99%	98%	96%	74%

The transmissivities of the B2B lens systems with 30  $\mu\text{m}$ , 50  $\mu\text{m}$ , and 80  $\mu\text{m}$  apertures are 31%, 34%, and 43% after removing the noise floor caused by the pyro-electric detector itself in the data of both beams. They are also influenced by the three factors mentioned in Section 4.1, from which we conclude that the dominant factor is the air gaps between the lenses and the wafer-piece. However, the B2B lens system with an aperture is more sensitive to the tilt angle than to the

offset because different incident angles cause changes in the directions of the refracted beams inside the silicon, which causes the focus to shift from the center of the silicon lens focal plane. Without an aperture, this influence is relatively small, but with an aperture, a small deviation of the focus from the center of the focal plane causes the light to be blocked. For the situation with an offset, the transmission loss is related to the increase on the light path inside the AR coating but the focus is still on the center of the silicon lens focal plane. To give an intuitive impression, the transmissivity changes for the B2B system with a 30  $\mu\text{m}$  aperture as a function of tilt angle and offset when the incoming beam is a fundamental Gaussian beam are simulated and plotted in Figs. 7(b) and 7(c), as indicated with blue lines. The transmissivity drops nearly to zero with a 2° tilt angle, which proves that there is still room to improve the transmissivity of the B2B lens with careful alignment in the measurements. Besides, the transmissivity is also impacted by the misalignment between the center of the lenses and the center of the aperture caused by the alignment procedure. Figure 7(d) plots the simulated transmissivity changes of the lens systems with 30  $\mu\text{m}$ , 50  $\mu\text{m}$ , and 80  $\mu\text{m}$  apertures as a function of the ratio between the misalignment and the aperture size when the input beam is a fundamental Gaussian one. Since the misalignments of the lens systems for 30  $\mu\text{m}$ , 50  $\mu\text{m}$ , and 80  $\mu\text{m}$  aperture are measured to be 2  $\mu\text{m}$ , 4  $\mu\text{m}$ , and 2  $\mu\text{m}$  respectively, these misalignments cause negligible influence on the transmissivity of the lens system.

The Gaussicity of the lens system is 99%, 98%, and 96% for 30  $\mu\text{m}$ , 50  $\mu\text{m}$ , and 80  $\mu\text{m}$ , respectively. The highest Gaussicity comes from the aperture size of 30  $\mu\text{m}$  although the differences between the three are small. All the Gaussicities of the output beams are considerably higher than that of the input beam, confirming that the B2B lens system can effectively filter a non-ideal input beam to a Gaussian beam and even close to a perfect Gaussian beam. The B2B lens system with 30  $\mu\text{m}$  aperture is most favorable for this QCL beam by taking both the Gaussicity and transmissivity into account.

QCLs do not usually generate an ideal beam. Therefore, an interesting question to know how much fundamental Gaussian component is contained in the non-ideal beam power. A by-product of our study with this QCL is to determine this quantity. When the output QCL beam is resized with two lenses, the B2B lens system with the 30  $\mu\text{m}$  aperture can filter and result in 31% power from the input beam to the fundamental Gaussian beam. However, we know a fundamental Gaussian beam will have a transmissivity of 80% by passing through the B2B lens system as simulated in Section 2.2, with a 20% loss. Therefore, this 31% should be divided by 0.8, leading to ~39% as the fundamental Gaussian component of the resized QCL beam. Unfortunately, we cannot determine the Gaussian component of the original QCL beam since its outer part was lost due to the limited diameter of the first lens.

No measurements have been performed to illustrate the broadband performance of the B2B lens system. However, we model the transmissivity of the B2B lens system (the AR coating is optimized for 3.86 THz) by varying the frequency of the incoming beam from 3 THz to 5.4 THz and we find a maximal drop of 10% within this frequency range. Therefore, we conclude that the B2B lens system has a wide bandwidth (at least 62%), which should be sufficient for most astronomical applications.

## 5. Conclusions

We report a novel THz spatial filter that consists of two back-to-back elliptical silicon lenses and an aperture in between, formed by a thin gold blocking layer on a silicon wafer-piece. Combining a designed mechanical lens holder and micro-manipulators, we can align the lenses and the aperture with an accuracy of 1  $\mu\text{m}$ . The performance of the lens system with and without aperture is experimentally characterized using a third order DFB QCL at 3.86 THz. When the input beam is Gaussian, the intensity profile of the output beam from the lens system without the gold layer is nearly the same as the input beam and the transmission of the lens system is measured to

be 72%, close to the simulated transmission of 80%. With a non-Gaussian beam as an input, the lens system with an aperture shows an output beam with a Gaussicity reaching 99% and a transmission of larger than 30% from the input beam. The latter depends also strongly on the input beam profile. Here we demonstrate the B2B lens system at 3.86 THz because of the availability of a source. This concept can be applied to any other THz frequencies by optimizing the AR coating thickness and adjusting the aperture size. Thus, we show that by combining a B2B lens system with a QCL, one can generate an LO with not only high output power but also a fundamental Gaussian beam. This is required for heterodyne receivers at supra-THz frequencies, in particular array receivers, for the airborne observatory of SOFIA [19], the coming balloon borne observatory of GUSTO [18], and the proposed space mission of Origins Space Telescope [48].

## Appendix A

Figures 9(a), 9(b), and 9(c) show a 3D model of the mechanical lens holder for our B2B lens system, its top view, and its cross-section, respectively. The mechanical lens holder is placed on a movable stage of an optical microscope, which is equipped with three micro-manipulators, allowing for fine tuning of the stage in two orthogonal directions. The three micro-manipulators equipped with digital displays have an accuracy of 1  $\mu\text{m}$ . The flat (or back) part of two lenses and both sides of the wafer-piece are cleaned with acetone and isopropyl alcohol in a clean-room environment to prevent particles on the surfaces. The bottom lens is first placed on the support

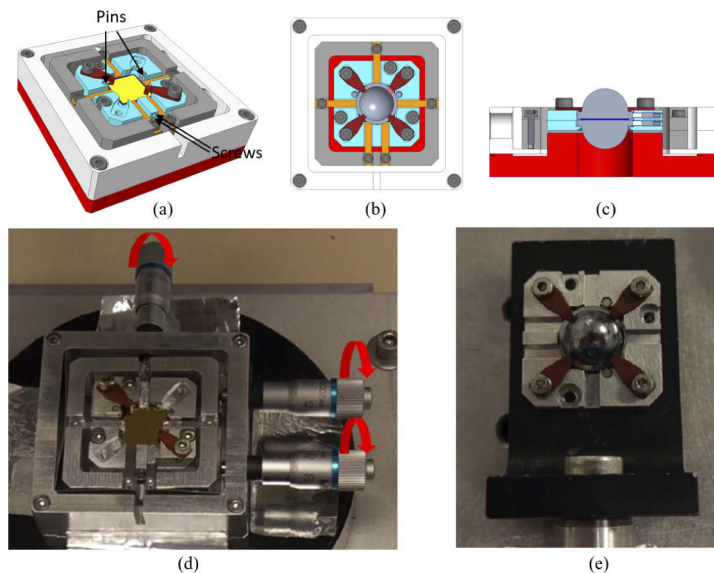


**Fig. 9.** (a) Designed 3D model of the mechanical lens holder. (b) Top view of the mechanical lens holder. (c) Cross-section of the mechanical lens holder. The flat parts of the lenses and the Si wafer-piece are cleaned and the bottom lens is placed on the blue structure. The Si wafer-piece is placed on top of the bottom lens and then the top lens is placed on top of the Si wafer-piece. (d) Real photo of the mechanical lens holder. Three micro-manipulators are used to adjust the position of the Si wafer-piece to make its center coincide with the center of the bottom lens. After aligning the centers of the lens and the wafer-piece, the wafer-piece is glued to the mechanical lens holder from the two corners without brown clips. (e) After aligning the two lenses and the Si wafer-piece, the outer part is removed and the inner part is used in an optical system.

structure in blue in Fig. 9. The structure in red under the blue only functions as a holder to prevent the bottom lens from potential damage. To fix the position of the bottom lens, a small screw next to the extension part of the lens is used to push it against the two small pins next to the wafer-piece. After the position of the bottom lens is fixed, the center of the bottom lens is found and marked by the crossline of the microscope eyepiece. Then, the wafer-piece is placed on top of the bottom lens and two brow clips on the diagonal positions are loosely fastened by two screws to push the wafer-piece down, leaving the other two corners for adding glue. The part in dark gray in Fig. 9(a) is movable and five metal strips shown in orange color are mounted on it. These five metal strips keep the wafer-piece in position by pushing it from all sides. The three micro-manipulators in Fig. 9(d) are used to move the dark gray part to change the position of the wafer-piece until the center of the aperture is in the same position as the center of the bottom lens. Then the wafer-piece is glued through the two corners without brown clips on the blue part. After the glue is dried, the two brown clips and five metal strips are removed and the top lens is placed on top of the wafer-piece. A screw next to its extension part is also used to push it against the two pins to make sure it is in the same position as the bottom lens, as in Fig. 9(b). Four brown clips are fastened by four screws and used to push the top lens down. Then the outer part of the blue structure is removed and the B2B lens system, as shown in Fig. 9(e), is ready for an optical test.

## Funding

China Scholarship Council (201706030153); Rijksuniversiteit Groningen; Technische Universiteit Delft; SRON Netherlands Institute for Space Research.

## Acknowledgments

We thank Paul Urbach at TU Delft for support and useful discussions, and Nuria Llombart Juan at TU Delft for suggesting the introduction of an aperture. We also thank Jan Geralt bij de Vaate at SRON for supporting Y. Gan's Ph.D. activities within the Instrument Science Group at SRON.

## Disclosures

The authors declare no conflicts of interest.

## References

1. C. K. Walker, *Terahertz Astronomy* (Taylor & Francis Group, 2016), Chap. 1.
2. R. Hussin, Y. Chen, and Y. Luo, "Thin-Film Single-Crystal Schottky Diodes for IR Detection and Beyond," *IEEE Trans. Electron Devices* **63**(10), 3971–3976 (2016).
3. W. Zhang, P. Khosropanah, J. R. Gao, E. L. Kollberg, K. S. Yngvesson, T. Bansal, R. Barends, and T. M. Klapwijk, "Quantum noise in a terahertz hot electron bolometer mixer," *Appl. Phys. Lett.* **96**(11), 111113 (2010).
4. H. Li, W. Wan, Z. Tan, Z. Fu, H. Wang, T. Zhou, Z. Li, C. Wang, X. Guo, and J. Cao, "6.2-GHz modulated terahertz light detection using fast terahertz quantum well photodetectors," *Sci. Rep.* **7**(1), 3452 (2017).
5. M. Rösch, G. Scalari, G. Villares, L. Bosco, M. Beck, and J. Faist, "On-chip, self-detected terahertz dual-comb source," *Appl. Phys. Lett.* **108**(17), 171104 (2016).
6. Z. Li, W. Wan, K. Zhou, X. Liao, S. Yang, Z. Fu, J. C. Cao, and H. Li, "On-Chip Dual-Comb Source Based on Terahertz Quantum Cascade Lasers Under Microwave Double Injection," *Phys. Rev. Appl.* **12**(4), 044068 (2019).
7. H. Li, Z. Li, W. Wan, K. Zhou, X. Liao, S. Yang, C. Wang, J. C. Cao, and H. Zeng, "Toward Compact and Real-Time Terahertz Dual-Comb Spectroscopy Employing a Self-Detection Scheme," *ACS Photonics* **7**(1), 49–56 (2020).
8. C. Risacher, R. Güsten, J. Stutzki, H.-W. Hübers, R. Aladro, A. Bell, C. Buchbender, D. Büchel, T. Csengeri, C. Duran, U. U. Graf, R. D. Higgins, C. E. Honingh, K. Jacobs, M. Justen, B. Klein, M. Mertens, Y. Okada, A. Parikka, P. Pütz, N. Reyes, H. Richter, O. Ricken, D. Riquelme, N. Rothbart, N. Schneider, R. Simon, M. Wienold, H. Wiesemeyer, M. Ziebart, P. Fusco, S. Rosner, and B. Wohler, "The upGREAT Dual Frequency Heterodyne Arrays for SOFIA," *J. Astron. Instrum.* **07**(04), 1840014 (2018).
9. J. L. Kloosterman, D. J. Hayton, Y. Ren, T. Y. Kao, J. N. Hovenier, J. R. Gao, T. M. Klapwijk, Q. Hu, C. K. Walker, and J. L. Reno, "Hot electron bolometer heterodyne receiver with a 4.7-THz quantum cascade laser as a local oscillator," *Appl. Phys. Lett.* **102**(1), 011123 (2013).

10. M. S. Vitiello, G. Scalari, B. Williams, and P. De Natale, "Quantum cascade lasers: 20 years of challenges," *Opt. Express* **23**(4), 5167–5182 (2015).
11. X. M. Wang, C. L. Shen, T. Jiang, Z. Q. Zhan, Q. H. Deng, W. H. Li, W. D. Wu, N. Yang, W. D. Chu, and S. Q. Duan, "High-power terahertz quantum cascade lasers with ~ 0.23 W in continuous wave mode," *AIP Adv.* **6**(7), 075210 (2016).
12. A. Khalatpour, J. L. Reno, and Q. Hu, "Phase-locked photonic wire lasers by  $\pi$  coupling," *Nat. Photonics* **13**(1), 47–53 (2019).
13. Y. Jin, J. L. Reno, and S. Kumar, "Phase-locked terahertz plasmonic laser array with 2 W output power in a single spectral mode," *Optica* **7**(6), 708–715 (2020).
14. A. Khalatpour, J. L. Reno, N. P. Kherani, and Q. Hu, "Unidirectional photonic wire laser," *Nat. Photonics* **11**(9), 555–559 (2017).
15. P. F. Goldsmith, *Quasioptical Systems—Gaussian Beam Quasioptical Propagation and Applications* (Wiley-IEEE, 1998), Chap. 2.
16. M. Hajenius, J. J. A. Baselmans, A. Baryshev, J. R. Gao, T. M. Klapwijk, J. W. Kooi, W. Jellema, and Z. Q. Yang, "Full characterization and analysis of a terahertz heterodyne receiver based on a NbN hot electron bolometer," *J. Appl. Phys.* **100**(7), 074507 (2006).
17. K. M. Zhou, W. Miao, Z. Lou, J. Hu, S. L. Li, W. Zhang, S. C. Shi, R. Lefevre, Y. Delorme, and T. Vacelet, "A 1.4 THz Quasi-Optical NbN Superconducting HEB Mixer Developed for the DATE5 Telescope," *IEEE Trans. Appl. Supercond.* **25**(3), 1–5 (2015).
18. P. Bernasconi, C. K. Walker, and C. Kulesa, "The GUSTO balloon mission," presented at the *42nd COSPAR Scientific Assembly*, Pasadena, California, USA, 14–22 July 2018.
19. C. Risacher, R. Gusten, J. Stutzki, H.-W. Hubers, D. Buchel, U. Graf, S. Heyminck, C. E. Honingh, K. Jacobs, B. Klein, T. Klein, C. Leinz, P. Putz, N. Reyes, O. Ricken, H.-J. Wunsch, P. Fusco, and S. Rosner, "First Supra-THz Heterodyne Array Receivers for Astronomy With the SOFIA Observatory," *IEEE Trans. Terahertz Sci. Technol.* **6**(2), 199–211 (2016).
20. B. Mirzaei, J. R. G. Silva, Y. C. Luo, X. X. Liu, L. Wei, D. J. Hayton, J. R. Gao, and C. Groppi, "Efficiency of multi-beam Fourier phase gratings at 1.4 THz," *Opt. Express* **25**(6), 6581–6588 (2017).
21. Y. Gan, B. Mirzaei, J. R. G. Silva, A. Khalatpour, Q. Hu, C. Groppi, J. V. Siles, F. van der Tak, and J. R. Gao, "81 supra-THz beams generated by a Fourier grating and a quantum cascade laser," *Opt. Express* **27**(23), 34192–34203 (2019).
22. B. Mirzaei, J. R. G. Silva, D. Hayton, C. Groppi, T. Y. Kao, Q. Hu, J. L. Reno, and J. R. Gao, "8-beam local oscillator array at 4.7 THz generated by a phase grating and a quantum cascade laser," *Opt. Express* **25**(24), 29587–29596 (2017).
23. U. U. Garf and S. Heyminck, "Fourier grating as submillimeter beam splitter," *IEEE Trans. Antennas Propag.* **49**(4), 542–546 (2001).
24. H. Richter, M. Wienold, L. Schrottke, K. Biermann, H. T. Grahn, and H. Hübers, "4.7-THz Local Oscillator for the GREAT Heterodyne Spectrometer on SOFIA," *IEEE Trans. Terahertz Sci. Technol.* **5**(4), 539–545 (2015).
25. A. A. Danylov, J. Waldman, T. M. Goyette, A. J. Gatesman, R. H. Giles, K. J. Linden, W. R. Neal, W. E. Nixon, M. C. Wanke, and J. L. Reno, "Transformation of the multimode terahertz quantum cascade laser beam into a Gaussian, using a hollow dielectric waveguide," *Appl. Opt.* **46**(22), 5051–5055 (2007).
26. R. Degl'Innocenti, Y. D. Shah, D. S. Jessop, Y. Ren, O. Mitrofanov, H. E. Beere, and D. A. Ritchie, "Hollow metallic waveguides integrated with terahertz quantum cascade lasers," *Opt. Express* **22**(20), 24439–24449 (2014).
27. A. W. M. Lee, Q. Qin, S. Kumar, B. S. Williams, Q. Hu, and J. L. Reno, "High-power and high-temperature THz quantum-cascade lasers based on lens-coupled metal-metal waveguides," *Opt. Lett.* **32**(19), 2840–2842 (2007).
28. W. J. Wan, H. Li, and J. C. Cao, "Homogeneous spectral broadening of pulsed terahertz quantum cascade lasers by radio frequency modulation," *Opt. Express* **26**(2), 980–989 (2018).
29. E. E. Orlova, P. M. Solyankin, A. A. Angeluts, A. Lee, O. G. Kosareva, I. A. Ozheredov, A. V. Balakin, V. A. Andreeva, N. A. Panov, and V. N. Aksenov, "Spatial filtering of radiation from wire lasers," *Laser Phys. Lett.* **14**(4), 045001 (2017).
30. H. Pu, C. H. Du, S. Pan, T. J. Huang, and P. K. Liu, "A Broadband Back-to-Back Corrugated Horn Structure for Gaussian Mode Filtering in Terahertz Band," in *Proceedings of IEEE Conference on Microwave and Millimeter Wave Technology (ICMMT)*, 2018, pp. 1–3.
31. B. N. Ellison, M. L. Oldfield, D. N. Matheson, B. J. Maddison, C. M. Mann, and A. F. Smith, "Corrugated Feedhorns at Terahertz Frequencies — Preliminary Results," *Fifth International Symposium on Space Terahertz Technology (ISSTT)*, 1994, pp. 851–860.
32. J. Pawley, *Handbook of Biological Confocal Microscopy* (Springer, 2006), Chap. 5.
33. . The Netherlands, "Sumipro Submicron Lathing BV", <https://www.sumipro.nl>.
34. D. F. Filipovic, S. S. Gearhart, and G. M. Rebeiz, "Double-Slot Antennas on Extended Hemispherical and Elliptical Silicon Dielectric Lenses," *IEEE Trans. Microwave Theory Tech.* **41**(10), 1738–1749 (1993).
35. A. Skalare, T. de Graauw, and H. van de Stadt, "A planar dipole array antenna with an elliptical lens," *Microw. Opt. Technol. Lett.* **4**(1), 9–12 (1991).
36. W. Zhang, P. Khosropanah, J. R. Gao, T. Bansal, T. M. Klapwijk, W. Miao, and S. C. Shi, "Noise temperature and beam pattern of an NbN hot electron bolometer mixer at 5.25 THz," *J. Appl. Phys.* **108**(9), 093102 (2010).

37. A. J. Gatesman, J. Waldman, M. Ji, C. Musante, and S. Yagvesson, "An Anti-Reflection Coating for Silicon Optics at Terahertz Frequencies," *IEEE Microw. Guid. Wave Lett.* **10**(7), 264–266 (2000).
38. H. W. Hüber, J. Schubert, A. Krabbe, M. Birk, G. Wagner, A. Semenov, G. Gol'tsman, B. Voronov, and E. Gershenzon, "Parylene anti-reflection coating of a quasi-optical hot-electron bolometric mixer at terahertz frequencies," *Infrared Phys. Technol.* **42**(1), 41–47 (2001).
39. M. Born and E. Wolf, *Principles of Optics: Electromagnetic Theory of Propagation, Interference and Diffraction of Light* (Pergamon, 1970), Chap. 1.
40. . From [38] the absorption coefficient of Parylene C is derived to be 27 cm<sup>-1</sup>, which is independent of frequency in the range 1 THz – 3 THz. The absorption coefficient of Parylene C linearly increases with frequency from 3 cm<sup>-1</sup> to 18 cm<sup>-1</sup> between 0.45 THz to 2.8 THz based on the work by Gatesman [37]. From Zhang's work the absorption coefficient of Parylene C is derived to be 7.17 cm<sup>-1</sup> at 5.25 THz [36]. Based on the numbers from above literature, we take 25 cm<sup>-1</sup> as the absorption coefficient of Parylene C.
41. D. Grischkowsky, S. Keiding, M. van Exter, and C. Fattinger, "Far-infrared time-domain spectroscopy with terahertz beams of dielectrics and semiconductors," *J. Opt. Soc. Am. B* **7**(10), 2006 (1990).
42. COMSOL Multiphysics, <https://www.comsol.com/rf-module>.
43. When the incoming beam and the lens diameter rescale proportionally, the beam size on the center remains the same for 4 mm and 10 mm diameter lenses due to the law of light refraction. And this is also verified using Eqs. (3)–(5).
44. J. W. Goodman, *Introduction to Fourier Optics* (McGraw-Hill, 1968), Chap. 3.
45. . One condition for the first Rayleigh–Sommerfeld diffraction formula is that the diffracting fields must not be observed too close to the aperture. So the field in the xy plane is used instead of the field in the plane  $\Sigma$ .
46. . The Gaussities of the beams are derived by fitting the intensity values into the Gaussian equation using the curve fitting tool in Matlab. An R-square (also known as Coefficient of Determination) statistic is used to determine the quality of the fitting.
47. J. Miles, "R Squared, Adjusted R Squared," *J. Appl. Behav. Sci.* **4**, 1655–1657 (2005).
48. M. C. Wiedner, I. Mehdi, A. Baryshev, V. Belitsky, V. Desmaris, A. DiGiorgio, J.-D. Gallego Puyol, M. Gerin, P. Goldsmith, F. Helmich, W. Jellema, A. Laurens, C. Risacher, A. Cooray, and M. Meixner, "A Proposed Heterodyne Receiver for the Origins Space Telescope," *IEEE Trans. Terahertz Sci. Technol.* **8**(6), 558–571 (2018).